Monitoring the Phase Formation of Co-Evaporated Lead Halide Perovskite Thin Films by *in situ* XRD

Paul Pistor, Juliane Borchert, Wolfgang Fränzel, René Csuk, Roland Scheer*

Martin-Luther-Universität Halle-Wittenberg, Von-Danckelmann-Platz 3, 06120 Halle (Saale), Germany

AUTHOR INFORMATION

Corresponding Author

*Corresponding author: Paul Pistor, electronic mail: paul.pistor@physik.uni-halle.de

ABSTRACT Perovskite solar cells based on $(CH_3NH_3)Pb(I,Cl)_3$ have recently demonstrated rapidly increasing cell efficiencies. Here, we show progress identifying phases present during the growth of $(CH_3NH_3)Pb(I,Cl)_3$ perovskite thin films with the vacuum-based co-evaporation approach using two sources under varying deposition conditions. With *in situ* X-ray diffraction, crystalline phases can be identified and monitored in real time. For different $(CH_3NH_3)I$ to $PbCl_2$ flux ratios, 2 distinct $(CH_3NH_3)Pb(I_xCl_{(1-x)})_3$ phases with high ($x>0.95$) and with lower ($x<0.5$) iodine content as well as a broad miscibility gap in-between were found. During post deposition annealing we observe recrystallization and preferential orientation effects and finally the decomposition of the perovskite film to PbI_2 at temperatures above 200°C.

TOC GRAPHICS

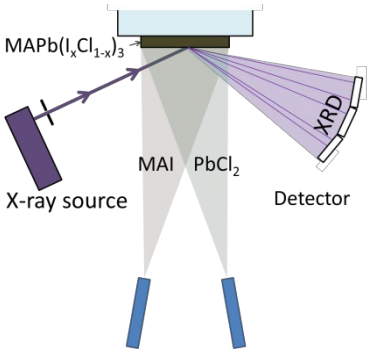

KEYWORDS $(CH_3NH_3)Pb(I,Cl)_3$, Perovskite Solar Cells, in situ XRD, Crystalline Phases, Recrystallization, Decomposition, Photovoltaic

With the prospect of a novel hybrid low cost and highly efficient solar cell technology, organic-inorganic perovskite semiconductors based on $(CH_3NH_3)Pb(I,Cl)_3$ have recently entered into the focus of the photovoltaic research community. Processed by various low cost solution- and vacuum-based technologies, this new thin film material with high direct absorption, a tunable band gap and high open circuit voltages above 1 V has made an impressive progress with ever increasing power conversion efficiencies rapidly approaching 20% within few years. [1, 2, 3, 4]

The mineral perovskite ($CaTiO_3$) lends its name to the homonymous class of materials with similar cubic crystal structure and general chemical formula ABX_3. Organic-inorganic lead halide perovskites have drawn scientific attention already for some decades because of their hybrid organic-inorganic character and singular opto-electronic properties [5, 6] and their synthesis and crystal structure have been studied in detail. [7, 8, 9, 10] However, the potential of

methylammonium (MA) lead iodide and related hybrid perovskites as light harvesting materials was only realized when they were used as a sensitizer in dye-sensitized solar cells for the first time in 2009 [11] and rapid success in employing them in different solar cell device configurations thereafter. [12] While the perovskite $MAPb(I,Cl)_3$ was primarily used as a dye in dye-sensitized solar cells because of its high direct light absorption, the discovery of its excellent charge transport properties led to rapid modifications of the cell design and power conversion efficiencies surpassing 10% in 2012. [13, 14] Since then, scientific interest and efforts have exploded and reported record efficiencies more than doubled within only two years. [4]

Efficiencies well above 15% have been obtained by several approaches with varying absorber compositions and charge transport materials as well as different device architectures. [1]

Most perovskite solar cell absorbers so far have been deposited via solution-based wet-chemical processes in mesoscopic solar cell designs, [15] but vacuum-based planar approaches have also been successfully implemented with similar efficiencies. [16, 17, 18] Vacuum-based co-evaporation techniques allow the growth of high quality crystalline thin films under very well-defined conditions and their analysis *in situ*.

For single crystals and powders, the crystal structures of MA lead halides $MAPbX_3$ (X=I, Br, Cl) have been studied in detail, [7, 8] and a cubic perovskite structure with space group Pm3m at high temperatures and a transition to tetragonal phases with lower symmetry at decreasing transition temperatures from I (+57 °C) to Br (-36.9 °C) to Cl (-96.0 °C) were found. [9, 10] But with respect to thin film depositions, phase formations under varying process conditions are far more complex and much less understood so far. However, the reproducible growth of homogenous and well-defined absorber layers is crucial for the performance of the device and depends on a detailed

knowledge of possibly involved phases as well as their interaction and dependence on process conditions.

This was the motivation for the design of a dedicated vacuum chamber for perovskite thin film deposition by multi-source evaporation. The system is equipped with various process controlling facilities including a quartz microbalance, a laser light scattering (LLS) and an *in situ* X-ray diffraction (XRD) setup. The chamber is a copy of a setup used for the detailed monitoring of phase formation in multi-stage chalcopyrite and kesterite thin film growth. Further details on the system can be found in reference 19. The XRD system is operated with a Cu X-ray source at a fixed incident angle of 12.5° and a position-sensitive detector array covering the 2Θ diffraction angle range from 11° to 38°. The power of *in situ* XRD lies in the time-resolved analysis of the formation of crystalline phases during film growth. Detailed observation of the XRD peak pattern, changes in peak intensities and positions reveal information on the crystalline phases present, their growth and decrease as well as on compositional shifts, thus allowing the adjustment of process parameters even during the process. Before taking out the samples of the chamber a fingerprint of the deposition process is obtained and often an estimate of the crystalline quality of the film can be given. It is also a valuable tool to study time-resolved degradation and decomposition mechanisms under controlled conditions.

In this work we show with *in situ* XRD the evolution of different crystalline phases during thin film growth by co-evaporating methylammonium iodide (MAI) and lead chloride ($PbCl_2$). We demonstrate how different process parameters, namely the MAI to $PbCl_2$ flux ratio, lead to the deposition of distinct crystalline $MAPb(I,Cl)_3$ phases. In addition, we monitor recrystallization and decomposition of $MAPb(I,Cl)_3$ thin films into PbI_2 upon thermal heating.

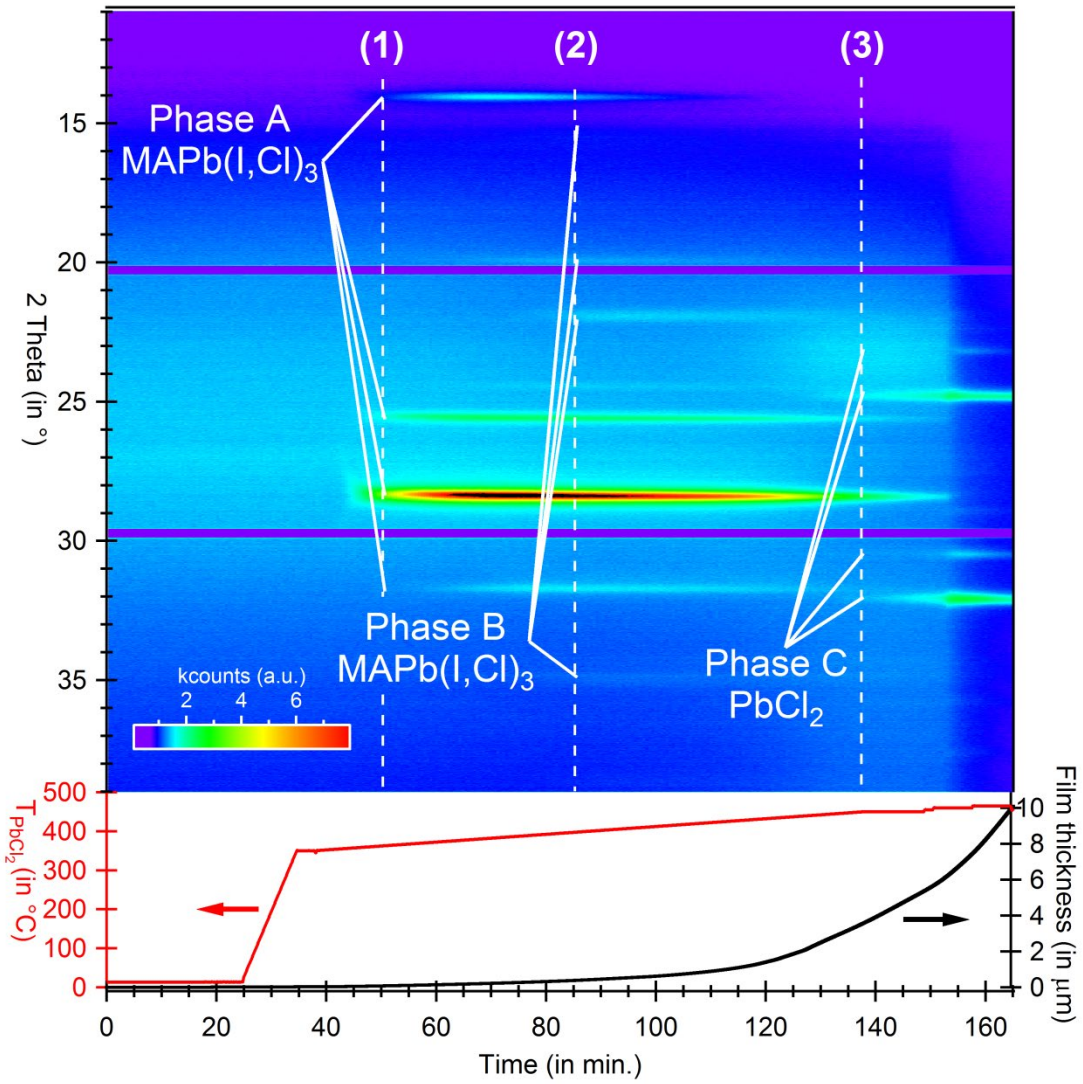

Figure 1. Color-coded representation of the diffracted intensity measured during $MAPb(I,Cl)_3$ formation. Three different crystalline phases named A, B and C can be detected in different growth regimes marked with dotted lines (1), (2) and (3), respectively. For comparison, the temperature ramp of the $PbCl_2$ crucible and the deposited film thickness as marked by the quartz microbalance are depicted below.

MAI and $PbCl_2$ were evaporated onto unheated soda-lime glass substrates in a high vacuum chamber with a base pressure in the order of or below 10^{-5} mbar. When solely the $PbCl_2$ source was heated, the quartz microbalance detected a continuous $PbCl_2$ deposition for crucible temperatures above 330°C. As a consequence, the $PbCl_2$ deposition rate could be controlled and calibrated with the quartz microbalance as usual. To the contrary, no thin film deposition could be detected with the microbalance upon heating the MAI source alone. Instead, the chamber pressure increased significantly for MAI crucible temperatures above 100°C. For well-defined $MAPb(I,Cl)_3$ depositions we therefore monitored the chamber pressure as a control for the MAI supply. We operated the MAI source at a constant temperature of 110°C leading to a pressure in the range of $2x10^{-4}$ mbar to $3x10^{-4}$ mbar.

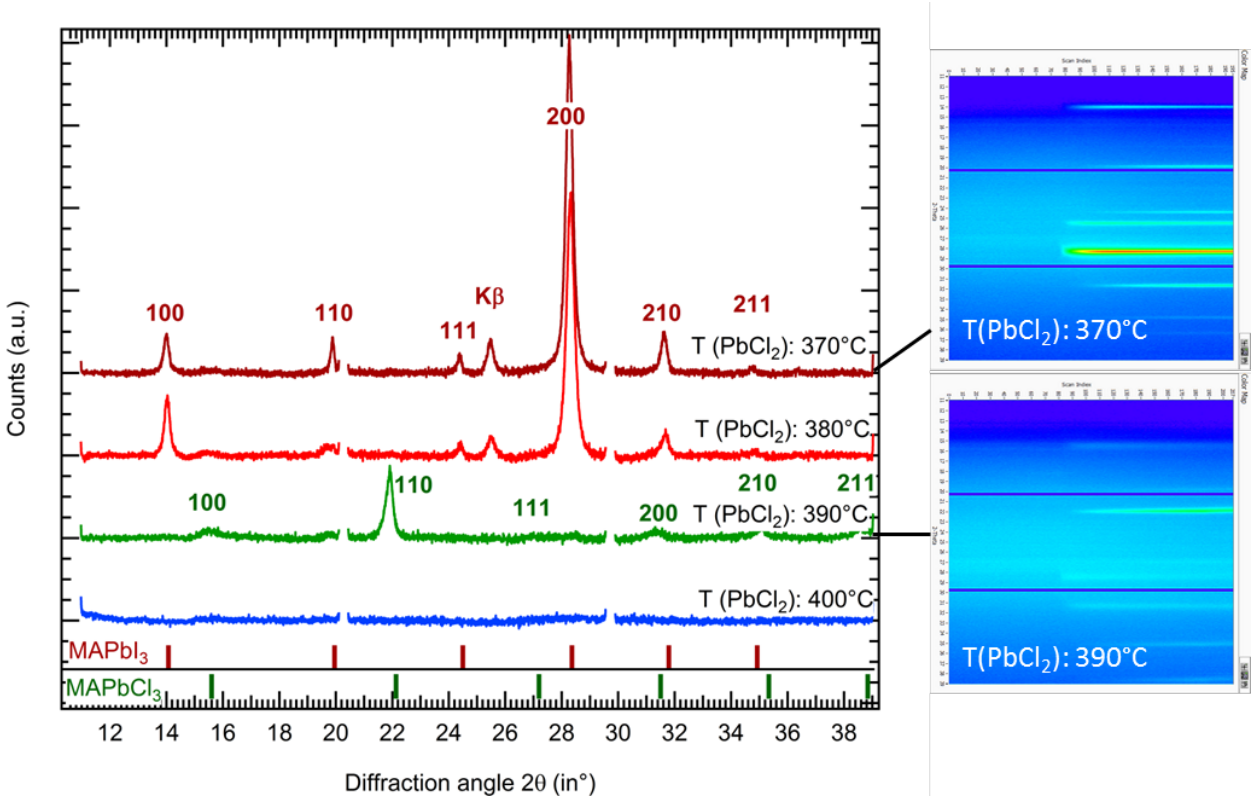

Figure 2. X-ray diffraction data for $MAPb(I,Cl)_3$ thin films grown with different $PbCl_2$ crucible

temperatures and consequently increasing $PbCl_2$ fluxes. The Bragg peak positions corresponding to literature data for cubic $MAPbI_3$ [10] and cubic $MAPbCl_3$ [9] are marked as bars below.

The formation of different crystalline phases on the substrate was found to depend critically on the applied MAI to $PbCl_2$ flux ratio. Figure 1 shows the color-coded representation of X-ray diffraction data recorded during the deposition of $MAPb(I,Cl)_3$. During this process, the $PbCl_2$ rate was continuously increased by increasing the crucible temperature from 350°C to 465°C. Three different growth regimes can be distinguished and are marked with dotted lines in the colormap. In the beginning (1), a crystalline phase named A with intense Bragg peaks at 14.046(6)°, 25.579(9)°[†], 28.332(2)° and 31.69(3)° is observed. For higher $PbCl_2$ crucible temperatures, the intensity of these Bragg peaks decreases and a second crystalline phase B is formed with peaks at 15.40(9)°, 19.71(6)°, 21.89(4) and 35.05(4)°. Upon further increase of the $PbCl_2$ rate finally a third phase C is formed with peaks at 23.22(4)°, 24.804(8)°, 30.44(1)° and 32.125(6)°, which can be easily identified as excess $PbCl_2$ deposited on the substrate. The other two phases A and B have perovskite crystal structure with the general formula $MAPb(I_xCl_{1-x})_3$. They can reproducibly be obtained for depositions with either low or high $PbCl_2$ fluxes, respectively. Figure 2 shows XRD data of four $MAPb(I,Cl)_3$ films separately obtained at different, constant $PbCl_2$ crucible temperatures between 370°C and 400°C, corresponding to deposition rates in the range between 1 Å/s to 2 Å/s. The upper two traces ($PbCl_2$ temperature of 370°C and 380°C) show the phase A crystallization. At a constant $PbCl_2$ temperature of 390°C, a film in phase B configuration is formed. Finally, for even higher crucible temperatures, no XRD peaks could be detected even after prolonged depositions. Because the response of the laser light

[†]The peak at 25.579° is a contribution of the Cu Kβ excitation.

signal indicated the deposition of a film we assume the deposition of an amorphous thin film for these conditions.

Films deposited at low $PbCl_2$ fluxes (phase A) were opaque and dark grey/brown for thicknesses of 500-700 nm. Optical transmission/reflection measurements revealed a band gap of ~1.60eV, close to the band gap expected for $MAPbI_3$ (approximately 1.55 eV) [14]. Films in phase B configuration with similar thickness visually appeared greenish and transparent. Scanning electron micrographs showed continuous and homogenous thin films for lowest and highest $PbCl_2$ fluxes and crater-like inhomogeneities for intermediate $PbCl_2$ fluxes. The elemental composition of the thin films was analyzed by energy dispersive X-ray spectroscopy. The results confirmed the lead to halide ratios of the general formula $MAPb(I_xCl_{1-x})_3$ and are displayed in Table 1. Films deposited with low $PbCl_2$ fluxes (phase A) exhibited only very low chloride contents with x between 0.98 and 0.95, while all films in phase B configuration showed high chloride contents with x around 0.5.

Despite the fact that pure $MAPbI_3$ is known to crystallize in a tetragonal structure at room temperature, all XRD peaks we observed for phase A can be indexed corresponding to the cubic modification of $MAPbI_3$ [10]. Additional peaks that would be characteristic for the tetragonal modification as the 211 peak at 23.47° or the splitting of the cubic 200 into the tetragonal 004/220 peaks were not observed. As a strong preferential orientation of the thin films can impede the detection of certain peaks, a powder was prepared from a thin film in phase A configuration by scratching off the film from the substrate. Again, clear indications for the tetragonal symmetry were missing in the XRD analysis of the obtained $MAPb(I,Cl)_3$ powder material (see supplementary materials for more details). We expect the incorporation of Cl into $MAPb(I,Cl)_3$ to effectively lower the cubic-tetragonal transition temperature and stabilize the

cubic modification at room temperature. More detailed data on the $MAIPbI_3$-$MAPbCl_3$ system and its phases is desirable to elucidate this point. For practical concerns avoiding multiple phase transitions under working conditions might have a positive influence on cell stability in the long term for solar cell applications.

Despite the high Iodine content detected by EDX measurements, the XRD data obtained for phase B matches well the literature data for the pure cubic $MAPbCl_3$, [9] only slightly shifted to lower diffraction angles (e.g. the 110 peak by 0.24°). Both phases, A and B, can therefore be described as cubic perovskites with space group Pm3m (No. 221) but with different lattice constants. Films grow either in the first or in the second configuration, triggered very sensibly by the $PbCl_2$ flux but probably also dependent on other parameters kept constant in our experiments, e.g. substrate temperature and MAI flux. While the halide perovskites $MAPb(I_yBr_{1-y})_3$ are reported to form a solid solution over the whole range of compositions from $MAPbI_3$ to $MAPbBr_3$ ($0<y<1$), [24] the presented results strongly suggest that the mixed $MAPb(I_xCl_{1-x})_3$ perovskites are not stable for all mixtures between $MAPbI_3$ and $MAPbCl_3$. Based on our data we estimate this miscibility gap to be in the regime between $0.95 > x > 0.50$, which is important when considering different process routes or tuning opportunities for the fabrication of solar cell absorbers in the future. It also helps to understand the generally very low reported Cl contents ($x \sim 0.97$) for wet-chemically processed $MAPb(I_xCl_{1-x})_3$ absorbers. [22, 23] This might tentatively be explained by the increasing difference in the I-Br-Cl ionic radii and has already been indicated in density functional theory calculations by Mosconi and co-workers. [25] The observed shift in XRD peak positions of the phase B configuration with respect to the calculated positions from reported pure $MAPbCl_3$ data seems quite small considering the large amount of iodine detected in our films by EDX. It has to be noted that the composition of the whole thin film is probed by EDX,

which in the presence of secondary amorphous phases might differ from the composition of the crystalline phases detected by XRD. As a consequence, the miscibility gap for $MAPbI_3$-$MAPbCl_3$ mixtures might be even wider than the one indicated by the abrupt change in composition and crystal structure found in our experiments.

Table 1. Details of the observed crystalline phases A and B.

Phase	$MAPb(I_xCl_{1-x})_3$ composition(EDX)				Match of XRD datawith literature Space group: cubic Pm3m			Appearance	$PbCl_2$ flux
	Pb (%)	I (%)	Cl (%)	x	Compound	Ref.	Lattice parameter a		
A	21.7	76.6	1.7	0.98	$MAPbI_3$	(10)	~6.288 Å	Opaque	Low
B	24.8	34.9	40.3	0.46	$MAPbCl_3$	(9)	~5.675 Å	Transparent, green	High

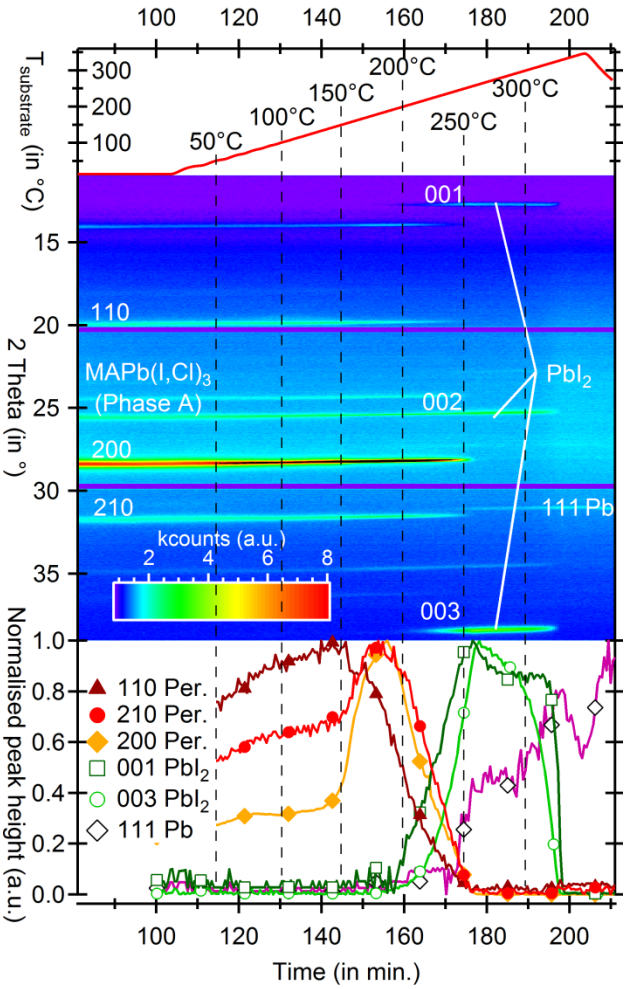

Figure 3. Structural evolution of a $MAPb(I,Cl)_3$ thin film upon thermal heating after the growth. Upper graph: Substrate temperature profile during the heating process. Middle graph: Color-coded representation of the in situ XRD data during heating. Lower graph: Evolution of the Bragg peak height for the 110, 210, 200 peaks of the $MAPb(I,Cl)_3$ perovskite (filled markers), the 001, 003 peaks of PbI_2 (empty squares and circles) and the 111 peak of elemental Pb (empty diamonds).

Additionally, we investigated the effect of thermal treatments on the $MAPb(I,Cl)_3$ thin films after their growth. Fig. 3 summarizes the observed structural changes as well as the process

parameters. A $MAPb(I,Cl)_3$ thin film was grown with low chlorine content as described above (phase A). The deposited thin film was then heated in vacuum with a linear temperature ramp in 100 min. from 15 °C up to 350 °C. In the color-coded representation of the XRD data, first an increase in intensity can be observed up to a temperature of approximately 150°C. The three representative Bragg peaks (110, 200, 210) depicted below show a comparable increase in peak height for all three peaks, accompanied by a decrease in their full width at half maximum (not displayed). This is interpreted as a recrystallization improving the crystallite size and crystalline quality of the films. Most publications on high efficiency devices prepared at low temperatures report on similar annealing steps in the temperature range between 100°C and 150°C. [16, 26, 13, 4] We therefore believe this recrystallization to be necessary to fundamentally improve thin film quality and to reduce structural defects. The observed peak intensities indicate a preferential 200 orientation of the as grown thin film. This preferential orientation is enhanced upon further annealing, as the 200 peak intensity is increasing, opposite to the intensity of the 110 peak, for example. Strong preferential orientations have already been reported for wet-chemically processed $MAPb(I,Cl)_3$ thin films, with much stronger orientation for films containing Cl than corresponding pure $MAPbI_3$ thin films. [14, 21, 22] Above approximately 200°C, all perovskite peaks decrease rapidly and the thin film is decomposed into PbI_2. Finally, when surpassing temperatures of approximately 330°C, the PbI_2 is removed leaving only small traces of elemental Pb on the substrate. The decomposition of $MAPb(I,Cl)_3$ thin films into PbI_2 has been reported previously by several groups and can be thermally triggered and enhanced by humidity and light exposure. [27, 28, 29, 24] The decomposition at these relatively low temperatures is an indication for the relative instability of the perovskite material, which might turn out to be a critical point for the technological implementation of this technology.

In conclusion, we were able to monitor changes in and the formation of crystalline phases under varying process conditions in real-time during thin film growth. We could resolve different perovskite phases during the deposition of $MAPb(I,Cl)_3$ thin films depending critically on the MAI / $PbCl_2$ flux ratio. For low $PbCl_2$ fluxes and unheated substrates, we detected black $MAPb(I_xCl_{1-x})_3$ perovskite films with high iodine content (x>95%) and a bandgap of approximately 1.6 eV. For higher $PbCl_2$ fluxes the transition to a different, transparent $MAPb(I_xCl_{1-x})_3$ perovskite phase with higher Cl content occurs (x~0.5). The results indicate a miscibility gap for the $MAPbI_3$ and $MAPbCl_3$ phases in the investigated regime ($0.5<x<0.95$), which would explain the low Cl contents found in previous studies on solution-processed $MAPb(I_xCl_{1-x})_3$ thin films. They help to control the difficulties and understand the complexity that can be encountered during co-evaporation as used for today´s highest-efficiency planar perovskite solar cells based on $MAPb(I_x,Cl_{1-x})_3$.

During a thermal heating of the deposited $MAPb(I_{0.98},Cl_{0.02})_3$ perovskite recrystallization and texturing of the thin film at temperatures below 200°C and a decomposition to PbI_2 for higher temperatures could be monitored *in situ* and in real time by XRD. This experiment elucidates the necessity for a post deposition annealing at temperatures in the range between 100°C-150°C, as applied to most low-temperature processed perovskite solar cells.

Acknowledgement:

We would like to thank Mr. Björn A. Weber for his valuable help in the preparation of some starting materials and Mr. Stefan Hartnauer for technical help setting up the equipment.

Supporting Information Available:

XRD powder data of the scratched films. This material is available free of charge via the

Internet at http://pubs.acs.org.

References:

(1) Boix, P. P.; Nonomura, K.; Mathews, N.; Mhaisalkar, S. G. Current Progress and Future Perspectives for Organic/Inorganic Perovskite Solar Cells. *Materials Today* **2014,** *17* , 16-23.

(2) Snaith, H. J. Perovskites: The Emergence of a New Era for Low-Cost, High-Efficiency Solar Cells. *The Journal of Physical Chemistry Letters* **2013,** *4*, 3623-3630.

(3) Green, M. A.; Emery, K.; Hishikawa, Y.; Warta, W.; Dunlop, E. D. Solar Cell Efficiency Tables (version 44). *Prog. Photovolt: Res. Appl.* **2014,** *22*, 701-710.

(4) Zhou, H.; Chen, Q.; Li, G.; Luo, S.; Song, T.-b.; Duan, H.-S.; Hong, Z.; You, J.; Liu, Y.; Yang, Y. Interface Engineering of Highly Efficient Perovskite Solar Cells. *Science* **2014,** *345*, 542-546.

(5) Wasylishen, R. E.; Knop, O.; Macdonald, J. B. Cation Rotation in Methylammonium Lead Halides. *Solid State Communications* **1985,** *56*, 581-582.

(6) Onoda-Yamamuro, N.; Matsuo, T.; Suga, H. Dielectric Study of $CH_3NH_3PbX_3$ (X = Cl, Br, I). *Journal of Physics and Chemistry of Solids* **1992,** *53*, 935-939.

(7) Mitzi, D. B. *Chapter: Synthesis, Structure, and Properties of Organic-Inorganic Perovskites and Related Materials;* **Progress in Inorganic Chemistry,** Volume 48, Wiley-Blackwell, 1999; pp 1-121.

(8) Mitzi, D. B. Thin-Film Deposition of Organic-Inorganic Hybrid Materials. *Chemistry of Materials* **2001,** *13*, 3283-3298.

(9) Kawamura, Y.; Mashiyama, H. Modulated Structure in Phase II of $CH_3NH_3PbCl_3$. *Journal of the Korean Physical Society* **1999,** *35,* 1437.

(10) Kawamura, Y.; Mashiyama, H.; Hasebe, K. Structural Study on Cubic-Tetragonal Transition of $CH_3NH_3PbI_3$. *J. Phys. Soc. Jpn.* **2002,** *71*, 1694-1697.

(11) Kojima, A.; Teshima, K.; Shirai, Y.; Miyasaka, T. Organometal Halide Perovskites as Visible-Light Sensitizers for Photovoltaic Cells. *Journal of the American Chemical Society* **2009,** *131*, 6050-6051.

(12) Im, J.-H.; Lee, C.-R.; Lee, J.-W.; Park, S.-W.; Park, N.-G. 6.5% Efficient Perovskite Quantum-Dot-Sensitized Solar Cell. *Nanoscale* **2011,** *3*, 4088.

(13) Kim, H.-S.; Lee, C.-R.; Im, J.-H.; Lee, K.-B.; Moehl, T.; Marchioro, A.; Moon, S.-J.; Humphry-Baker, R.; Yum, J.-H.; Moser, J. E.; et al. Lead Iodide Perovskite Sensitized All-Solid-State Submicron Thin Film Mesoscopic Solar Cell with Efficiency Exceeding 9%. *Sci. Rep.* **2012,** *2,* 591,.

(14) Lee, M. M.; Teuscher, J.; Miyasaka, T.; Murakami, T. N.; Snaith, H. J. Efficient Hybrid Solar Cells Based on Meso-Superstructured Organometal Halide Perovskites. *Science* **2012,** *338*, 643-647.

(15) Burschka, J.; Pellet, N.; Moon, S.-J.; Humphry-Baker, R.; Gao, P.; Nazeeruddin, M. K.; Grätzel, M. Sequential Deposition as a Route to High-Performance Perovskite-Sensitized Solar Cells. *Nature* **2013,** *499*, 316-319.

(16) Liu, M.; Johnston, M. B.; Snaith, H. J. Efficient Planar Heterojunction Perovskite Solar Cells by Vapour Deposition. *Nature* **2013,** *501*, 395-398.

(17) Hu, H.; Wang, D.; Zhou, Y.; Zhang, J.; Lv, S.; Pang, S.; Chen, X.; Liu, Z.; Padture, N. P.; Cui, G. Vapour-Based Processing of Hole-Conductor-Free $CH_3NH_3PbI_3$ perovskite/C60 fullerene planar solar cells. *RSC Adv.* **2014**, 4, 28964-28967

(18) Chen, Q.; Zhou, H.; Hong, Z.; Luo, S.; Duan, H.-S.; Wang, H.-H.; Liu, Y.; Li, G.; Yang, Y. Planar Heterojunction Perovskite Solar Cells via Vapor Assisted Solution Process. *Journal of the American Chemical Society* **2014,** *136,* 622-625.

(19) Kaune, G.; Hartnauer, S.; Scheer, R. In situ XRD Investigation of $Cu_2ZnSnSe_4$ Thin Film Growth by Thermal Co-Evaporation. *physica status solidi (a)* **2014,** Early View, DOI: 10.1002/pssa.201330340.

(20) Baikie, T.; Fang, Y.; Kadro, J. M.; Schreyer, M.; Wei, F.; Mhaisalkar, S. G.; Graetzel, M.; White, T. J. Synthesis and Crystal Chemistry of the Hybrid Perovskite $(CH_3NH_3)PbI_3$ for Solid-State Sensitised Solar Cell Applications. *J. Mater. Chem. A* **2013,** *1*, 5628.

(21) Edri, E.; Kirmayer, S.; Henning, A.; Mukhopadhyay, S.; Gartsman, K.; Rosenwaks, Y.; Hodes, G.; Cahen, D. Why Lead Methylammonium Tri-Iodide Perovskite-Based Solar Cells Require a Mesoporous Electron Transporting Scaffold (but Not Necessarily a Hole Conductor). *Nano Letters* **2014,** *14*, 1000-1004.

(22) Colella, S.; Mosconi, E.; Fedeli, P.; Listorti, A.; Gazza, F.; Orlandi, F.; Ferro, P.; Besagni, T.; Rizzo, A.; Calestani, G.; al., e. $MAPbI_{3-x}Cl_x$ Mixed Halide Perovskite for Hybrid Solar

Cells: The Role of Chloride as Dopant on the Transport and Structural Properties. *Chemistry of Materials* **2013**, *25*, 4613-4618

(23) Zhao, Y.; Zhu, K. CH_3NH_3Cl-Assisted One-Step Solution Growth of $CH_3NH_3PbI_3$: Structure, Charge-Carrier Dynamics, and Photovoltaic Properties of Perovskite Solar Cells. *The Journal of Physical Chemistry C* **2014,** *118*, 9412-9418

(24) Noh, J. H.; Im, S. H.; Heo, J. H.; Mandal, T. N.; Seok, S. I. Chemical Management for Colorful, Efficient, and Stable Inorganic-Organic Hybrid Nanostructured Solar Cells. *Nano Lett.* **2013,** *13,* 1764-1769.

(25) Mosconi, E.; Amat, A.; Nazeeruddin, M. K.; Graetzel, M.; De Angelis, F. First-Principles Modeling of Mixed Halide Organometal Perovskites for Photovoltaic Applications. *The Journal of Physical Chemistry C* **2013,** *117*, 13902-13913.

(26) Ball, J. M.; Lee, M. M.; Hey, A.; Snaith, H. J. Low-Temperature Processed Meso-Superstructured to Thin-Film Perovskite Solar Cells. *Energy \& Environmental Science* **2013,** *6*, 1739.

(27) Supasai, T.; Rujisamphan, N.; Ullrich, K.; Chemseddine, A.; Dittrich, T. Formation of a Passivating $CH_3NH_3PbI_3/PbI_2$ Interface During Moderate Heating of $CH_3NH_3PbI_3$ Layers. *Appl. Phys. Lett.* **2013,** *103*, 183906

(28) Tan, K. W.; Moore, D. T.; Saliba, M.; Sai, H.; Estroff, L. A.; Hanrath, T.; Snaith, H. J.; Wiesner, U. Thermally Induced Structural Evolution and Performance of Mesoporous Block Copolymer-Directed Alumina Perovskite Solar Cells. *ACS Nano* **2014,** *8,* 4730-4739.

(29) Ito, S.; Tanaka, S.; Manabe, K.; Nishino, H. Effects of Surface Blocking Layer of Sb_2S_3 on Nanocrystalline TiO_2 for $CH_3NH_3PbI_3$ Perovskite Solar Cells. *Journal of Physical Chemistry C* **2014,** *118*, 16995-17000